JOURNAL OF THERMOPHYSICS AND HEAT TRANSFER
Vol. 20, No. 3, July–September 2006

Heating Environments of a Venus Entry Capsule in a Trail Balloon Mission

Kazuhisa Fujita* and Takahiro Sumi†
Institute of Space Technology and Aeronautics, Japan Aerospace Exploration Agency, Tokyo 182-8522, Japan
and
Tetsuya Yamada‡ and Nobuyuki Ishii§
Institute of Space and Astronautical Science, Japan Aerospace Exploration Agency, Kanagawa 229-8510, Japan

A preliminary assessment of the heating environments during a hyperbolic entry to the planet Venus is conducted to investigate fundamental characteristics of flows in the shock layer and to predict the convective and radiative heat flux transferred to the entry capsule at the peak-heating point. Thermochemical nonequilibrium flows are calculated using two-dimensional Navier–Stokes equations in the axisymmetric geometry, taking into account oxidation and sublimation of the heatshield surface, and pyrolysis-gas injection. Radiative heat transfer coupled with the flow is computed by a line-by-line method with a tangent-slab approximation. Influences of uncertainties in the thermochemical models on the predicted heat flux are also examined.

Nomenclature

D_0	=	dissociation energy measured from the lowest vibrational level, J/mol
k	=	Boltzmann constant, 1.381×10^{-23} J/K
m	=	mass of particle, kg
$\dot{m}$	=	mass injection rate, kg/m$^2 \cdot$ s
$\dot{m}_p$	=	pyrolysis-gas injection rate, kg/m$^2 \cdot$ s
$\dot{m}^C$	=	rate of mass formation in chemical reactions on wall, kg/m$^2 \cdot$ s
$\dot{m}^P$	=	mass injection rate due to pyrolysis-gas injection, kg/m$^2 \cdot$ s
q	=	heat flux, W/m^2
S_r	=	radiative heat of formation per unit volume and time, J/m$^3 \cdot$ s
T	=	temperature, K
T_a	=	rate-control temperature, K
z	=	local coordinate normal to wall, m
α	=	reaction probability
Γ	=	diffusion flux directed outward from wall, kg/m$^2 \cdot$ s
ϵ	=	coefficient of spontaneous emission, W/m$^3 \cdot$ sr $\cdot$ Å
$\bar{\epsilon}_v$	=	average removed vibrational energy at dissociation, J/mol
θ	=	angle between z coordinate and line of light, rad
κ'	=	coefficient of absorption including induced emission, 1/m
λ	=	wavelength, Å
ρ	=	mass density, kg/m^3

Subscripts

c, r	=	convective and radiative heat flux, respectively
i, j	=	running indices for chemical species
w	=	wall

Superscripts

$+, -$	=	forward and backward flux, respectively

I. Introduction

THE planet Venus has a variety of conditions, attracting a lot of interest among astronomers, geoscientists, and meteorologists.[1] Historically, not many probe vehicles have been sent to this planet so far; however, 15 years have already passed since the last encounter by the Magellan explorer in 1990. More recently, a Venus Express mission[2] was launched in 2005 by the ESA to investigate the Venusian atmosphere, the plasma environments, and the surface characteristics of Venus from orbit. Likewise, the Japan Aerospace Exploration Agency (JAXA) is planning a Venus climate orbiter[3] for launch in 2008 to investigate the Venusian atmosphere from a planetary meteorological viewpoint.

To explore the atmospheric planets, it is often more advantageous to send entry probes into the atmosphere and to perform in situ measurements. From this viewpoint, at JAXA, fundamental research of atmospheric planetary entry has been conducted to improve planetary exploration technologies for future missions. With respect to Venus, which has anomalous meteorological phenomena, planetary balloons hovering in the atmosphere for a long period are expected to work as an effective platform for in situ sensing to gain aerononomical and meteorological information. For this reason, as one of candidates for the mission target, a conceptual study of a Venus trail balloon mission using an entry capsule is currently being undertaken.[4]

The primary purpose of this study is to extend our technology for predicting flight environments during atmospheric entry, acquired for Earth reentry in the MUSES-C mission,[5] to those for other planets. In this paper, the computational fluid dynamic (CFD) code and the radiation code are improved for Venusian entries and applied to an entry capsule of a Venus trail balloon mission. Influences of uncertainties in the thermochemical models on the predicted heat flux are also discussed.

II. Entry Capsule of Venus Balloon Mission

The Venus trail balloon mission is designed as a low-cost planetary exploration using a small vehicle system, with the mass of the entire system and the entry capsule including the balloon being 160 and 35 kg, respectively. To eliminate the propellant mass required to decelerate the vehicle, the capsule is designed to be flown into the Venusian atmosphere directly from an interplanetary hyperbolic orbit at an entry velocity over 11 km/s. After the capsule is decelerated to an equilibrium descent velocity, a balloon is ejected from

Presented as Paper 2005-5207 at the AIAA 38th Thermophysics Conference, Toronto, ON, 6–9 June 2005; received 14 June 2005; revision received 11 September 2005; accepted for publication 12 September 2005.

*Senior Researcher, Aerodynamics Research Group, 7-44-1 Jinidaiji-higashi-machi; kazudom@chofu.jaxa.jp. Senior Member AIAA.
†Aerospace Project Researcher, Aerodynamics Research Group. Member AIAA.
‡Research Associate, Research Division for Space Systems Engineering.
§Associate Professor, Research Division for Space Systems Engineering.

the capsule and deployed. The target altitude for balloon hovering ranges from 40 to 60 km, which is lower than those of the Vega balloons,[6] for the purpose of long-term observations below clouds of H_2SO_4 for the first time. Lower limits of the altitude may be subject to the maximum operable temperature of the high-temperature electronics. More detailed descriptions of the Venus balloon mission may be found in Ref. 4.

To reduce mass and complexity of the entire system, it is advantageous to deploy the balloon by the vapor pressure of water stored inside the balloon using heat transferred from the ambient high-temperature atmosphere, instead of pressurization using a working gas contained in cylinders.[7] To actualize this successfully, it is necessary to maintain the temperature inside the capsule low so that the vapor pressure remains lower than the ambient pressure until the balloon is ejected from the capsule. That is, a more accurate estimation of the heating environments, the thermal response of the heatshield material, and the thermal behavior of the entire system than before should be achieved along the entry trajectory.

In Ref. 4, a preliminary thermal analysis along the entry trajectory was conducted by changing the ballistic coefficient of the entry capsule to estimate the heatshield thickness required to maintain the vapor pressure of water below the ambient pressure until the capsule descends to the target altitude, 60 km. It was shown that capsules with a small ballistic coefficients require larger heatshield thicknesses. This is because the total heat capacity of the heatshield should be increased because the flight time to the target altitude after the peak-heating point becomes long, resulting in a temperature rise behind the heatshield due to heat conduction. In contrast, an excessive increase in the ballistic coefficient is not favorable because the inertial force due to deceleration increases, resulting in an increase in structural weight to maintain structural strength. From this analysis, a bullet-cone-type capsule with a moderate ballistic coefficient was selected tentatively. The concept of the entry capsule is shown in Fig. 1. The fundamental configuration and mass property of the capsule are summarized in Table 1.

Using the capsule configuration and mass property given in Table 1, we calculated the capsule dynamics under the nominal entry conditions, an entry velocity of 11.6 km/s and a flight path angle of −15 deg at an altitude of 200 km. The results are shown in Fig. 2. The entry capsule decelerates in a short period of time, approximately 20 s, at altitudes between 80 and 90 km. The convective and radiative heat fluxes in Fig. 2b are those calculated by

Table 1 Fundamental configuration and mass property of entry capsule for Venus balloon mission

Parameter	Value
Total axial length, m	0.62
Front diameter, m	0.35
Rear diameter, m	0.50
Nose radius at stagnation point, m	0.40
Total mass, kg	35.0

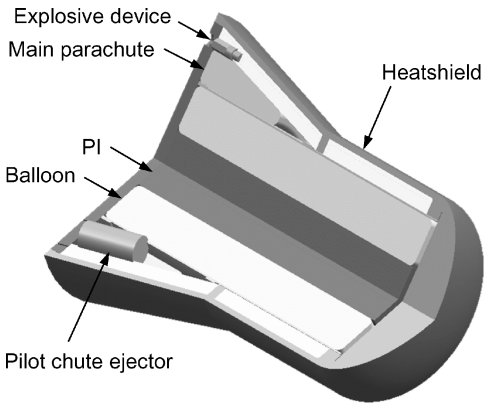

Fig. 1 Concept of entry capsule for Venus balloon mission.

Table 2 Flight conditions at peak-heating point

Parameter	Value
Altitude, km	89.4
Pressure, Pa	45.2
Temperature, K	173.8
Velocity, km/s	10.62

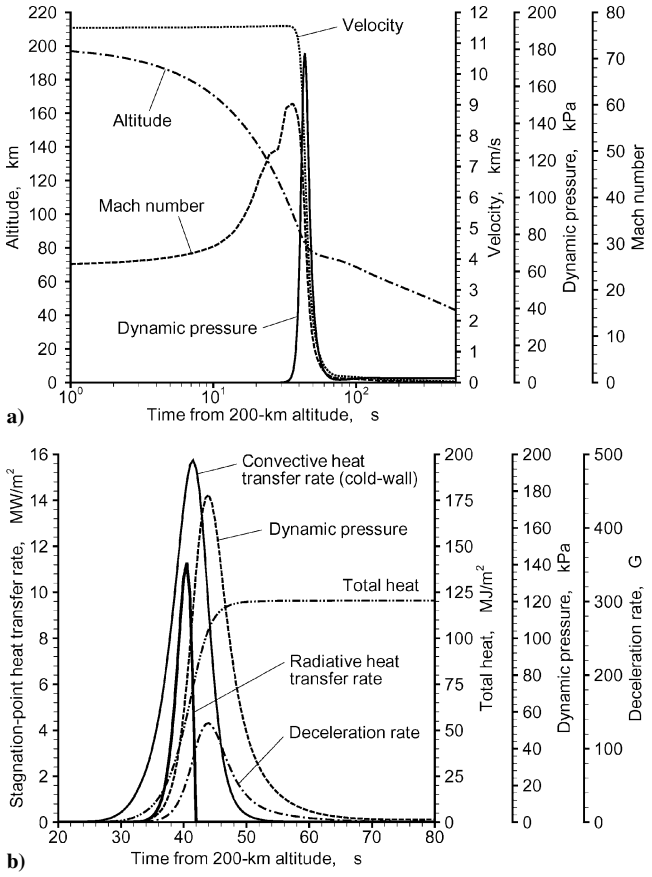

Fig. 2 Flight conditions along entry trajectory.

semi-empirical formulas[8,9] at the stagnation point. The peak-heating point is expected to be 40.5 s from the 200-km altitude. The flight conditions at the peak-heating point are summarized in Table 2.

III. Numerical Procedure

A. Thermochemical Models

Thermochemical models for reacting CO_2 flows were investigated and summarized in Refs. 9–12. More recently, several computations of shock-layer flows in Venusian entries, most of which are those of the Pioneer-Venus probes, were conducted by taking into account ablation, coupled radiation, and ablation-induced turbulence.[13–15] In the present study, the thermochemical, gasdynamic, and radiation models are introduced using the approaches listed just and are modified if necessary.

The Venusian atmosphere is assumed to consist of 97% CO_2 and 3% N_2 in mole concentration. Based on preliminary computations of the equilibrium and the nonequilibrium gas chemistry for shock-layer flows with ablation involved, we take into account 22 chemical species: H, C, N, O, H_2, C_2, N_2, CH, OH, CN, CO, NO, H_2O, C_2H, C_3, CO_2, e, C^+, O^+, O_2^+, CO^+, and NO^+, with 33 chemical reactions summarized in Table 3. The forward rate coefficient is calculated by $k_f = CT_a^n \exp(-E/T_a)$, where values of C, n, and E are given in Table 3. The backward rate coefficient is determined from k_f and the equilibrium constant, which is obtained from individual partition functions of chemical components involved in the reaction. The partition functions are calculated by the radiation code, SPRADIAN2 (Refs. 16 and 17), which is linked with the CFD code for radiation-coupled flowfield calculation. The forward rate coefficients given in

Table 3 Chemical reactions

Reaction no.	Reaction	Third body	C, $m^3/mol \cdot s$	n	E, K	Source
1	$H_2 + M \leftrightarrow H + H + M$	H_2	5.5×10^8	0.0	48,300	Ref. 12
		others	2.2×10^8	0.0	48,300	Ref. 12
2	$C_2 + M \leftrightarrow C + C + M$	All	3.7×10^8	0.0	69,900	Ref. 12
3	$N_2 + M \leftrightarrow N + N + M$	H, C, N, O	3.0×10^{16}	−1.6	113,200	Ref. 12
		e	3.0×10^{18}	−1.6	113,200	Ref. 12
		others	7.0×10^{15}	−1.6	113,200	Ref. 12
4	$CO + M \leftrightarrow C + O + M$	H, C, N, O	3.4×10^{14}	−1.0	129,000	Refs. 9, 10
		others	2.3×10^{14}	−1.0	129,000	Refs. 9, 10
5	$CH + M \leftrightarrow C + H + M$	All	4.8×10^{10}	−0.6	40,480	Ref. 9
6	$OH + M \leftrightarrow O + H + M$	All	4.8×10^{10}	−0.6	51,500	Ref. 9
7	$CN + M \leftrightarrow C + N + M$	All	2.5×10^8	0.0	87,740	Ref. 12
8	$NO + M \leftrightarrow N + O + M$	H, C, N, O, NO, CO_2	1.1×10^{11}	0.0	75,460	Refs. 9, 10
		others	5.0×10^9	0.0	75,460	Refs. 9, 10
9	$CO_2 + M \leftrightarrow CO + O + M$	H, C, N, O	1.4×10^{16}	−1.5	63,275	Refs. 9, 10
		others	6.9×10^{15}	−1.5	63,275	Refs. 9, 10
10	$H_2O + M \leftrightarrow OH + O + M$	All	8.2×10^{16}	−2.0	60,000	Ref. 9
11	$C_3 + M \leftrightarrow C_2 + C + M$	H, C, N, O	1.4×10^{16}	−1.5	87,740	Ref. 9
		others	6.9×10^{15}	−1.5	87,740	Ref. 9
12	$CO + C \leftrightarrow C_2 + O$	——	2.0×10^{11}	−1.0	58,000	Ref. 12
13	$CO + H \leftrightarrow CH + O$	——	2.5×10^7	0.5	88,440	Ref. 9
14	$CO + N \leftrightarrow CN + O$	——	1.0×10^8	0.0	38,600	Ref. 12
15	$N_2 + C \leftrightarrow CN + N$	——	1.1×10^8	−0.11	23,200	Ref. 12
16	$N_2 + O \leftrightarrow NO + N$	——	5.7×10^6	0.42	42,938	Ref. 12
17	$CN + O \leftrightarrow NO + C$	——	1.6×10^7	0.1	14,600	Ref. 12
18	$CN + C \leftrightarrow C_2 + N$	——	5.0×10^7	0.0	13,000	Ref. 12
19	$H_2O + C \leftrightarrow CH + OH$	——	7.0×10^2	1.5	18,800	Ref. 9
20	$H_2O + O \leftrightarrow OH + OH$	——	4.7×10^{12}	−1.0	17,000	Ref. 9
21	$CO + C_2 \leftrightarrow C_3 + O$	——	1.0×10^6	0.0	41,200	Ref. 12
22	$C_2H + H \leftrightarrow C_2 + H_2$	——	1.6×10^7	0.15	14,600	This work
23	$C_3 + C \leftrightarrow C_2 + C_2$	——	1.0×10^6	1.0	16,400	This work
24	$C_3 + N \leftrightarrow CN + C_2$	——	1.0×10^6	0.0	34,200	Ref. 12
25	$N + O \leftrightarrow NO^+ + e$	——	8.8×10^2	1.0	31,900	Ref. 10
26	$C + O \leftrightarrow CO^+ + e$	——	8.8×10^2	1.0	33,100	Ref. 10
27	$O + O \leftrightarrow O_2^+ + e$	——	7.1×10^{-4}	2.7	80,600	Ref. 10
28	$C + e \leftrightarrow C^+ + e + e$	——	3.7×10^{25}	−3.0	130,720	Ref. 12[a]
29	$O + e \leftrightarrow O^+ + e + e$	——	3.9×10^{27}	−3.78	158,500	Ref. 12
30	$NO^+ + C \leftrightarrow NO + C^+$	——	1.0×10^7	0.0	23,200	Ref. 10
31	$NO^+ + N \leftrightarrow N_2 + O^+$	——	3.4×10^7	−1.08	12,800	Ref. 10
32	$NO^+ + O \leftrightarrow N + O_2^+$	——	7.2×10^6	0.29	48,600	Ref. 10
33	$CO + C^+ \leftrightarrow CO^+ + C$	——	1.0×10^7	0.0	31,400	Ref. 10

[a]Another rate coefficient for the reaction 28 found in Refs. 10 and 9 is apparently in error, which is smaller than that of Ref. 12 by the order of magnitude.

Refs. 9, 10, and 12 are examined, and modifications are introduced to those for reactions 22 and 23 based on the existing experimental data.[18–20] This is because the rate coefficients for these reactions were only estimated in Ref. 12 from analogous reactions. The rate coefficients selected in the present work are compared with the existing experimental data in Fig. 3.

The two-temperature approximation[10] and the Landau–Teller-type relaxation model are used for vibrational relaxation with the relaxation parameters recommended in Ref. 10. At high temperatures, a correction is introduced using an imaginary cross section of elastic collisions as proposed in Ref. 10. In addition, a correction factor is introduced to the Landau–Teller model to take into account diffusive nature of vibrational relaxation at high temperatures (see Ref. 21). Relaxation between the translational and the electronic mode is assumed to occur by the shielded coulombic elastic collisions among charged particles. To take into account the preferential dissociation from high vibrational levels,[21] the average removed vibrational energy at dissociation is given by $\bar{\epsilon_v} = 0.3 D_0$.

B. Transport Properties

The coefficients of viscosity, thermal conductivity, and ordinary diffusion in a gas mixture are computed by the first-order expressions of Chapman–Enskog theory (see Ref. 22) with modifications to take into account in the ambipolar electric field.[23] The collision integrals used for this computation are mostly taken from recent publications.[12,24,25]

C. Ablation

Because calculation of ablation processes coupled with the flow is costly, thermochemical behavior of the carbon fiber reinforced plastics (CFRP) heatshield was calculated apart from the flowfield calculation. The wall temperature and the pyrolysis-gas injection rate obtained from this calculation are given to flow calculations as the boundary conditions on the wall surface. As shown in Fig. 2, the profiles of the cold-wall convective and radiative heat flux, and the temperature and equilibrium chemical composition at the stagnation pressure, were estimated along the entry trajectory. One-dimensional time-dependent equations governing the ablation processes were integrated in time using these profiles, for example, see Ref. 26.

The estimated wall temperature and the pyrolysis-gas injection rate at the peak-heating point were found to lie between 2750 and 3250 K and 0.10 and 0.30 $kg/m^2 \cdot s$, respectively, depending on the choice of uncertain physical parameters such as the Lewis number and the heating argumentation level.[26] From these results, three wall temperatures of 2750, 3000, and 3250 K, and two pyrolysis-gas injection rates of 0.1 and 0.3 $kg/m^2 \cdot s$, are tested in this study. The pyrolysis-gas released from the surface is assumed, following Ref. 5, to consist of 59.2% C, 13.1% H, and 27.7% O in mass concentration and to be in equilibrium at the wall at the wall temperature and pressure. Condensation into solid carbon is neglected because injected gases are in the decomposition phase. Calculated mole fractions of chemical components contained in the pyrolysis gas are summarized in Table 4. Dominant chemical components in the pyrolysis gas are H_2, CO, and H.

Table 4 Mole fractions of chemical components contained in pyrolysis gas at 1.47 atm

T, K	H	H_2	C_2	CO	H_2O	C_2H	C_3	CO_2
2750	0.045	0.652	0.000	0.182	0.000	0.026	0.095	0.000
3000	0.101	0.604	0.001	0.177	0.000	0.027	0.090	0.000
3250	0.191	0.527	0.003	0.169	0.000	0.026	0.084	0.000

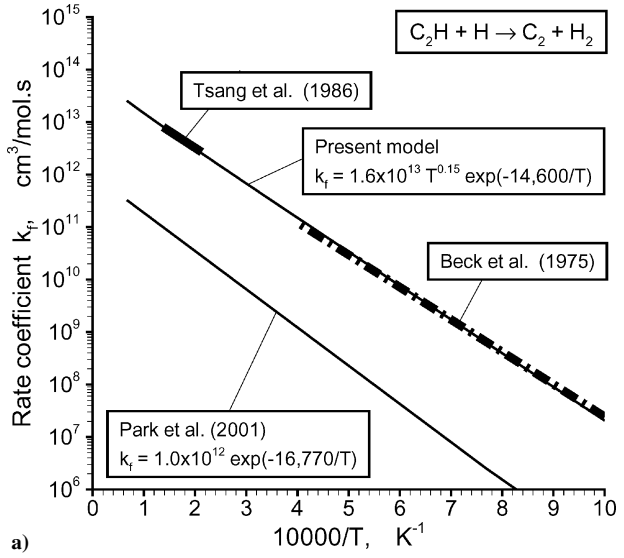

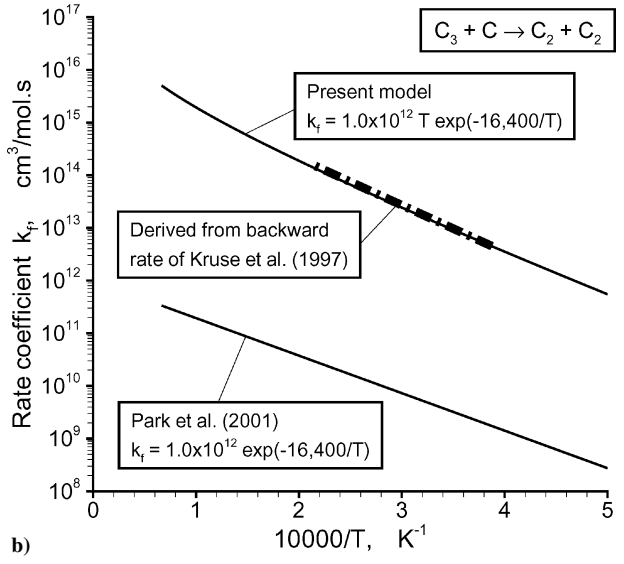

Fig. 3 Comparison between forward rate coefficients selected in present work and existing experimental data.[18–20]

Mass continuity of chemical species i on the wall interface is given in a general form as

$$\dot{m}_i = \dot{m}_i^P + \dot{m}_i^C = \Gamma_i + \rho_i(\alpha_i/4)\sqrt{8kT/\pi m_i} \tag{1}$$

Ionic species are assumed to recombine with an electron with a reaction probability of unity. For $i = C^+$, O^+, O_2^+, CO^+, and NO^+, Eq. (1) is reduced to

$$\dot{m}_i^P = \dot{m}_i^C = 0, \qquad 0 = \Gamma_i + \rho_i \tfrac{1}{4}\sqrt{8kT/\pi m_i} \tag{2}$$

and for $i = C^+$, O^+, and O_2^+,

$$\dot{m}_j^C = (m_j/m_i)\rho_i \tfrac{1}{4}\sqrt{8kT/\pi m_i} \tag{3}$$

where j is the parent neutral species of ionic species i. In this study, surface oxidation, $O + C(s) \rightarrow CO$, is taken into account for $i = O$. The probability of this reaction is taken from Ref. 9 as $\alpha_O = 0.63\exp(-1160/T)$. Equation (1) is reduced to

$$\dot{m}_O^P = 0 \qquad \dot{m}_O^C = \Gamma_O + \rho_O(\alpha_O/4)\sqrt{8kT/\pi m_O} \tag{4}$$

$$\dot{m}_{CO}^C = (m_{CO}/m_O)\rho_O(\alpha_O/4)\sqrt{8kT/\pi m_O} + (m_{CO}/m_{CO^+})\rho_{CO^+}\tfrac{1}{4}\sqrt{8kT/\pi m_{CO^+}} \tag{5}$$

In this study, nonequilibrium sublimation of C_3 is taken into consideration. According to Ref. 9, the mass injection rate of C_3 sublimation is given by

$$\dot{m}_{C_3}^C = \rho_{C_3}^E\left(\alpha_{C_3}/4\right)\sqrt{8kT/\pi m_{C_3}} \tag{6}$$

where $\rho_{C_3}^E = 6.84 \times 10^7 T^{-1}\exp(-59,410/T)$ kg/m^3 and $\alpha_{C_3} = 30\exp(-21,490/T)$. For $i = C_3$, Eq. (1) is rewritten as

$$\dot{m}_{C_3}^P = \Gamma_{C_3} + \left(\rho_{C_3} - \rho_{C_3}^E\right)\left(\alpha_{C_3}/4\right)\sqrt{8kT/\pi m_{C_3}} \tag{7}$$

For other neutral species i, the reaction probability is assumed to be zero. Equation (1) is reduced to

$$\dot{m}_i^P + \dot{m}_i^C = \Gamma_i \tag{8}$$

D. Radiative Heat Transfer

Radiative heat transfer is computed by a line-by-line method with a tangent-slab approximation in the wavelength range from 500 to 25,000 Å, using the radiation code SPRADIAN2 PL-6 (Ref. 17). Electronic transitions taken into account in this calculation are summarized in Table 5. Because H^+ and N^+ are not included in the CFD calculation, their concentrations are set to be zero to compute the absorption coefficients in the electronic bound-free transitions, $H + h\nu \rightarrow H^+$ and $N + h\nu \rightarrow N^+$, respectively. The two-temperature approximation is used in accordance with the CFD calculation.

Radiative heat of formation per unit volume and unit time, which is given to the energy equation for the CFD calculation as a source term, is defined by $S_r \equiv -\partial(q_r^+ + q_r^-)/\partial z$. The forward and the backward radiative flux are calculated by[16]

$$q_r^{\pm}(z) = -2\pi \int \mathrm{d}\lambda \int_0^{\pi/2} \sin\theta\, \mathrm{d}\theta \int_z^{(L\mp L)/2} \varepsilon(z', \lambda) \times \exp\left[-\int_z^{z'} \frac{\kappa'(z'', \lambda)}{\cos\theta}\, \mathrm{d}z''\right] \mathrm{d}z' \tag{9}$$

Table 5 Electronic transitions incorporated into SPRADIAN 2 in this study

Species	Transitions
	Atomic lines
H	215 transitions
C	1286 transitions
N	1091 transitions
O	885 transitions
C^+	651 transitions
O^+	857 transitions
	Molecular bands
H_2	$B \leftrightarrow X$, $C \leftrightarrow X$
C_2	$A \leftrightarrow X$, $D \leftrightarrow X$, $C \leftrightarrow A$, $E \leftrightarrow A$, $b \leftrightarrow a$, $d \leftrightarrow a$, $e \leftrightarrow a$
N_2	$A \leftrightarrow X$, $a \leftrightarrow X$, $b \leftrightarrow X$, $b' \leftrightarrow X$, $B \leftrightarrow A$, $C \leftrightarrow B$, $D \leftrightarrow B$
CH	$A \leftrightarrow X$, $B \leftrightarrow X$
OH	$A \leftrightarrow X$
CN	$A \leftrightarrow X$, $B \leftrightarrow X$
CO	$A \leftrightarrow X$, $B \leftrightarrow X$, $C \leftrightarrow X$, $E \leftrightarrow X$, $B \leftrightarrow A$, $b \leftrightarrow a$
NO	$A \leftrightarrow X$, $B \leftrightarrow X$, $C \leftrightarrow X$, $D \leftrightarrow X$
C_3	$A^1\Pi_u \leftrightarrow X^1\Sigma_g^+$, $S^1\Sigma_u^+ \leftrightarrow X^1\Sigma_g^+$
N_2^+	$A \leftrightarrow X$, $B \leftrightarrow X$, $C \leftrightarrow X$
CO^+	$A \leftrightarrow X$, $B \leftrightarrow X$
	Bound-free continua
H^+, C^+, N^+, O^+,O	$M^n + e \leftrightarrow M^{n-1} + h\nu$
	Free-free continua
N_2, N, O, ions	$M^n + e \leftrightarrow M^n + e + h\nu$

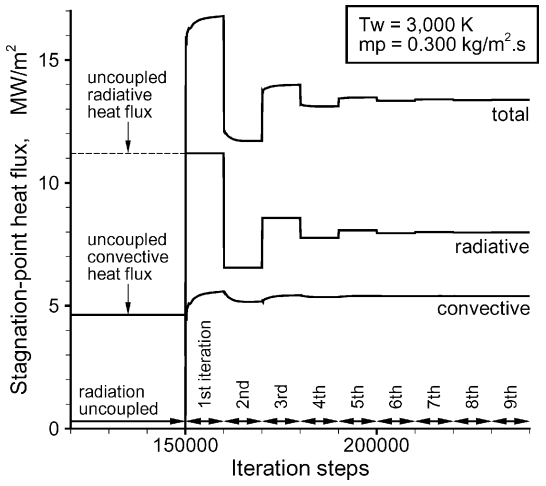

Fig. 4 Typical convergence history of stagnation-point heat flux in radiation-coupled flowfield calculation.

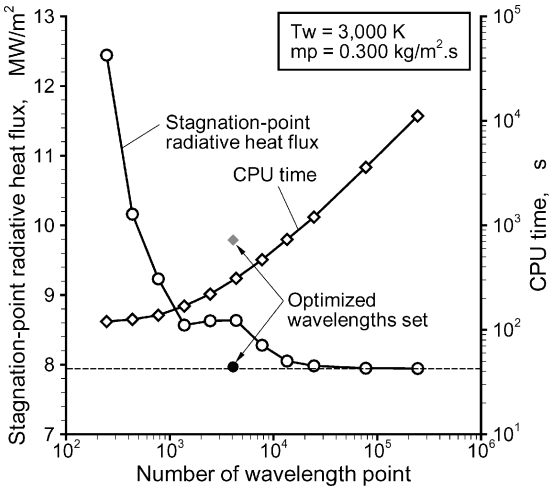

Fig. 5 Influence of wavelength discretization method on computed stagnation-point radiative heat flux and CPU time.

where $z = 0$ and L represent the wall surface and the outermost point from $z = 0$ along the local z coordinate, respectively. Emission from the high-temperature wall is represented by the blackbody radiation with a unique emissivity of 0.78 (Ref. 26), and taken into account in calculating the forward radiative heat flux. The radiative heat transfer is incorporated into the flow through an iterative procedure. First, the flowfield calculation without radiative heat transfer is performed. Radiative properties are then calculated from the flowfield results to determine S_r at each grid point of the computational domain, and the flowfield calculation is continued using the updated values of S_r. This procedure is repeated until both the convective and the radiative heat flux converge. In typical calculations, S_r was updated at every 10,000 steps of the CFD calculation. A typical convergence history is shown in Fig. 4 in terms of the heat flux monitored at the stagnation point.

Accuracy of the computed radiative heat flux depends significantly on the wavelength discretization method. That is, the radiative heat transfer calculation cannot be performed accurately unless line broadening of prominent spectral lines is resolved sufficiently. In Fig. 5, the radiative heat flux and the time required to perform one radiative-transfer calculation along the stagnation-point streamline are plotted against the number of wavelength points with a unique wavelength interval. Accuracy is improved as the wavelength resolution is enhanced; however, the computational time to process individual line shapes increases conversely. In this study, to reduce the computational cost without losing accuracy, the wavelength discretization method was optimized, and 4072 wavelength points with different intervals were selected. The heat flux computed with the selected wavelength points is, in general, within 0.3% errors compared to that obtained with 245,001 wavelength points at equal wavelength intervals of 0.1 Å, as seen in Fig. 5.

E. Method of Numerical Calculation

Because the capsule configuration and the flight trajectory have not been determined definitely, a simple hemisphere geometry with a nose radius of 0.4 m was assumed as the capsule nose configuration. The flowfield was assumed to be axisymmetric with respect to the stagnation-point streamline. To perform the radiation-coupled flowfield calculation, one numerical coordinate was aligned to the direction normal to the wall surface and the other to the tangential direction, with 101 and 25 grid points, respectively. Intervals between grid points were decreased in the normal direction in the vicinity of the wall to obtain sufficient accuracy in the computed heat transfer rate, based on preliminary studies on grid convergence. The cell Reynolds number based on the minimum grid interval is approximately unity.

The convective numerical flux was formulated by the AUSM-DV scheme[27] with the second-order upwind-biased MUSCL scheme.[28] To settle the strong stiffness originating from chemical reactions, the diagonal implicit scheme[29] was applied to the chemical source terms, whereas the convective and the viscous terms were integrated explicitly in time using local time steps. Calculations were made at the peak-heating point using the flow conditions given in Table 2.

IV. Numerical Results

A. Fundamental Characteristics of Flowfield

In Fig. 6, the distribution of temperatures and mole fractions of chemical components is plotted along the stagnation-point streamline for $T_W = 3000$ K and $\dot{m}_p = 0.3$ kg/m$^2 \cdot$ s. Significant thermochemical nonequilibrium is observed behind the shock wave and in the vicinity of the wall. Immediately behind the shock wave, CO_2 is seen to be dissociated quickly into CO and O, followed by vibrational relaxation and dissociation of CO. Primary electrons are produced mainly by reaction 27 behind the shock wave. When the electron temperature is sufficiently elevated through relaxation, C and O begin to be ionized by reactions 28 and 29, respectively. With a sufficient concentration of electrons at high temperatures, these reactions are very quick due to the avalanche effect (see Chap. 5 of Ref. 21). The concentration of C^+ and O^+ in the inviscid region of the shock layer is, therefore, not dependent on the reaction rate coefficient but on the equilibrium constant.

In the vicinity of the wall, the most dominant chemical component is CO, followed by H_2, H, and C. Spatial distribution of C_2 and C_3 is limited within a short distance from the wall, and their concentrations are relatively small in comparison with those of CO, H_2, and H. Such trends are different from those observed in Ref. 9. One reason is attributed to the forward rate coefficient of reaction 23, which is much higher in this calculation than in Ref. 9, as shown in Fig. 3b. A higher forward rate of this reaction decreases the concentration of C_3 more quickly toward the inviscid region. The second reason is that, under the flight conditions of Ref. 9, a considerable amount of H_2O and OH is injected from the wall because the pyrolysis gas consists of a larger amount of O (43.4% by mass) than in this calculation (27.7%).

B. Effect of Radiative Heat Transfer

In Fig. 7, the forward and the backward radiative heat flux and the radiative heat of formation obtained by the radiation-coupled calculation are plotted along the stagnation-point streamline for $T_w = 3000$ K and $\dot{m}_p = 0.3$ kg/m$^2 \cdot$ s. The radiative heat flux is seen to be absorbed in the vicinity of the wall and in the thermochemical nonequilibrium region immediately behind the shock wave, whereas the flow is cooled radiatively between these two regions. In Fig. 8, distributions of temperatures and dominant chemical components are compared with those obtained by the uncoupled calculation. In the presence of radiative heat transfer, temperatures in the shock layer are slightly decreased the inviscid region, especially a short distance from the wall, resulting in a decrease of the shock standoff

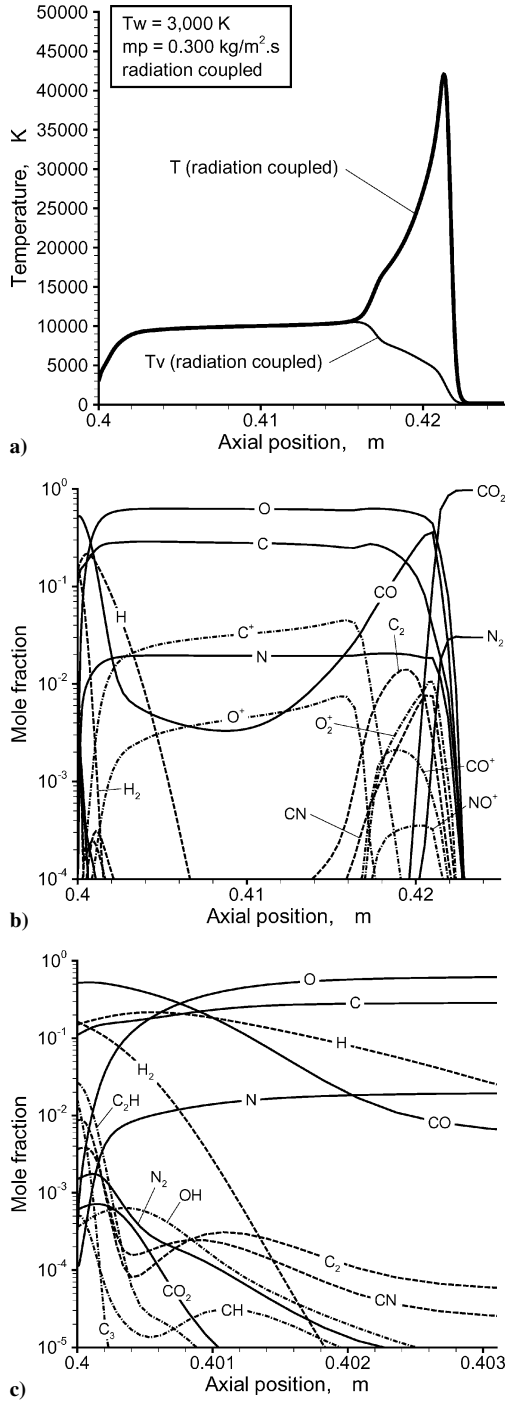

Fig. 6 Distribution of a) temperatures and b) and c) dominant chemical components along stagnation-point streamline for $T_w = 3000$ K and $\dot{m}_p = 0.3$ kg/m$^2 \cdot$ s.

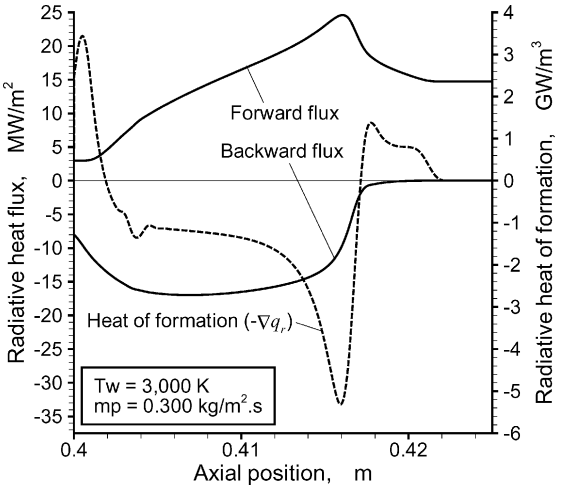

Fig. 7 Variation of forward and backward radiative heat flux and radiative heat of formation along stagnation-point streamline for $T_w = 3000$ K and $\dot{m}_p = 0.3$ kg/m$^2 \cdot$ s.

distance and a reduction in the radiative heat transfer rate. Conversely, as seen in Fig. 4, the convective heat transfer rate increases slightly because the temperature close to the wall is elevated due to absorption of the radiative heat flux. The degree of ionization decreases slightly in accordance with a temperature drop. Spatial distribution of chemical components is almost independent of the radiative heat transfer in the vicinity of the wall.

C. Radiation Spectra

The forward and the backward radiation spectra measured at the wall surface and ahead of the shock wave are shown in Figs. 9a and 9b, respectively. The maximum intensities of the forward and the backward radiation are enveloped approximately by the blackbody radiation at 9400 and 10,000 K, respectively. To illustrate the contribution of each chemical component to radiative heat transfer, distributions of total emission coefficients of individual electronic transitions are plotted along the stagnation-point streamline in Fig. 10. Distribution of the stagnation-point radiative heat flux among every 500-Å wavelength interval is shown in Fig. 11. From Figs. 10 and 11, we can conclude that the dominant sources of the radiative heat flux are atomic lines of C and O in vacuum-ultraviolet and ultraviolet wavelengths, followed by atomic lines of C^+, free-bound continua of C^+, and molecular band spectra of CO 4+ and C_2 Swan systems in the flight conditions under consideration.

In Fig. 12, spectral distribution of the absorption coefficient at a 0.47-mm distance from the wall is shown. In the flight conditions tested in this study, continuous absorption by molecular band systems of CO 4+, H_2 Lyman, and H_2 Werner, and by bound-free transitions of C, O, and H is dominant, in addition to line absorption of C and H. Because C_3, C_2, and H_2O are minor species existing only within a short distance from the wall, their contribution to absorption of the radiative heat flux was found to be negligibly small.

D. Stagnation-Point Heat Transfer Rate

The stagnation-point heat flux calculated with different conditions is summarized in Table 6. The cold-wall heat flux calculated for an imaginary fully catalytic wall (FCW) without ablation is also shown for comparison. A considerable reduction of the radiative heat flux is predicted by the radiation-coupled calculation even in the absence of ablation. In contrast, no reduction of the convective heat flux is brought about in the FCW case. This is because heat of formation due to recombination of the active species is most responsible for the convective heat transfer rate in the FCW case. The convective heat flux is found to be considerably reduced by ablation, as seen in Table 6.

Both in the radiation-coupled and uncoupled results, the radiative heat flux is almost independent of the wall temperature, whereas the convective heat flux decreases slightly as the wall temperature is elevated. In the radiation-uncoupled calculation, in general, the convective heat flux is underestimated, whereas the radiative heat flux is considerably overestimated, resulting in an overestimation of the total heat transfer rate. An increase of the pyrolysis-gas injection rate decreases the convective heat flux considerably, but the radiative heat flux only sightly, in the range of the pyrolysis-gas injection rate tested in this study.

V. Influences of Model Uncertainties

A. Tested Models

In Ref. 30, uncertainties in the thermal and chemical kinetic models for a reacting CO_2–N_2 mixture are discussed, and their influences on the computed radiative heat flux are examined. It was shown that,

Table 6 Stagnation-point heat transfer rates obtained by radiation-coupled and uncoupled calculations with different conditions, in megawatts per square meter

	$\dot{m}_p = 0.1$ kg/m$^2 \cdot$ s				$\dot{m}_p = 0.3$ kg/m$^2 \cdot$ s				FCW without ablation			
	Uncoupled		Coupled		Uncoupled		Coupled		Uncoupled		Coupled	
T_W (K)	q_c	q_r	q_c	q_r	q_c	q_r	q_c	q_r	q_c	q_r	q_c	q_r
300	——	——	——	——	——	——	——	——	16.2	14.3	16.1	9.7
2750	6.8	12.0	7.7	8.5	5.1	11.4	5.8	8.1	——	——	——	——
3000	6.6	12.0	7.5	8.5	4.6	11.2	5.4	8.0	——	——	——	——
3250	6.4	12.1	7.3	8.5	4.4	11.2	5.2	8.0	——	——	——	——

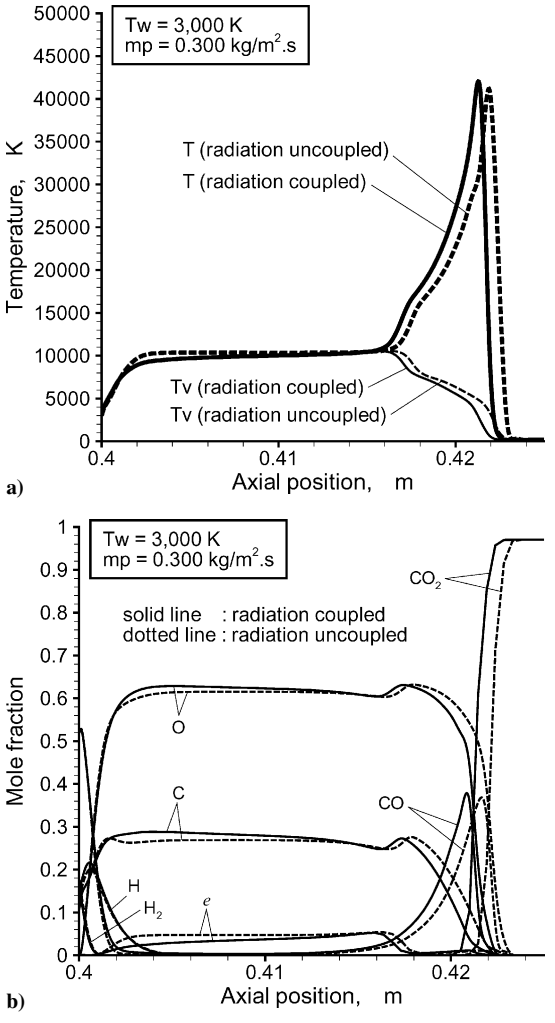

Fig. 8 Comparison between distributions of a) temperatures and b) dominant chemical components along stagnation-point streamline in radiation-coupled and uncoupled calculations.

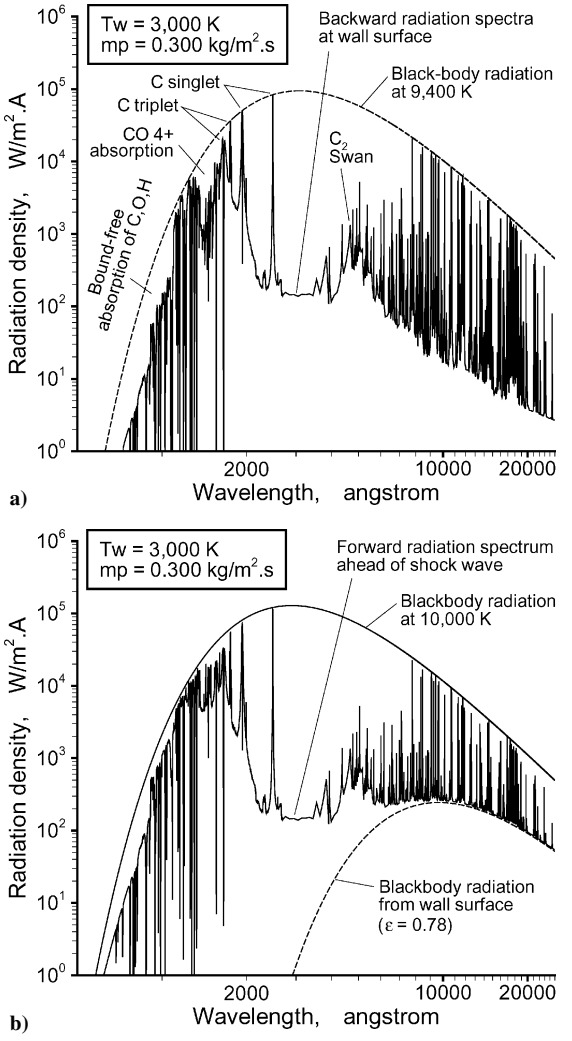

Fig. 9 Spectra of a) forward and b) backward radiative heat flux for $T_w = 3000$ K and $\dot{m}_p = 0.3$ kg/m$^2 \cdot$ s.

among such kinetic processes with uncertainties, dissociation of CO makes an significant impact on the computed radiative heat transfer rate. This is because the radiative heat flux depends on concentrations of the primary gas components, C, O, and CO, as seen in Fig. 10.

In Ref. 31, the rate coefficients of CO dissociation determined by different experiments are found to be scattered considerably by the order of magnitude. Recommended rate coefficients were deduced in Ref. 10 from the reaction rate measured in Ref. 32 for $M = $ Ar at 10,000 K, with an assumption that the third-body efficiencies for $M =$ atoms and molecules are 10 and 15, respectively. The dissociation rate coefficients so determined were demonstrated in Ref. 10 using the experimental data of Refs. 33 and 34 in terms of radiation intensity of the CO 4+ and C_2 Swan system, respectively. Unfortunately, no published data are available to make a thorough reexamination of the dissociation rate coefficient. Note that the third-body efficiencies are found to be identical among CO, C, and O in Ref. 34. From the preceding discussions, we consider that the rate coefficient of CO dissociation has an uncertainty of an order of magnitude. In Ref. 30, a significant increase in the radiative heat transfer rate was brought about in the absence of ablation and radiative heat transfer when the dissociation rate coefficient multiplied by 0.25 was tested. In this study, we test this dissociation rate in the presence of ablation and radiative heat transfer.

The rate coefficients for the reactions 22 and 23 in Ref. 12 are replaced in this study with new ones based on the experimental measurements.[18–20] To examine influences of these reaction rates on the thermochemical behavior of ablation gases and on the heat transfer rate, comparative calculations are also made using the rate coefficients given in Ref. 12.

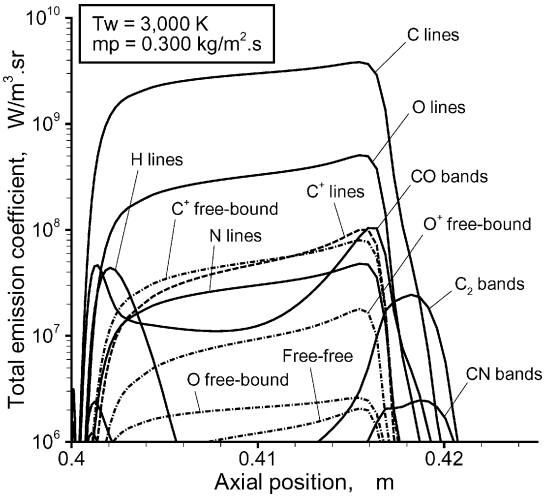

Fig. 10 Distribution of total emission coefficients of individual components along stagnation-point streamline for $T_w = 3000$ K and $\dot{m}_p = 0.3$ kg/m$^2 \cdot$ s.

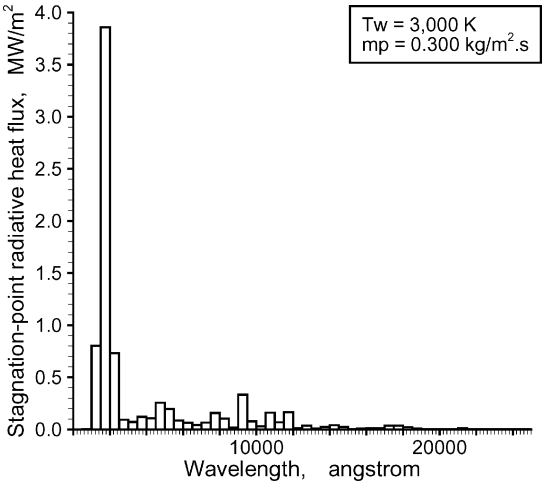

Fig. 11 Distribution of subtotal radiative heat flux at every 500-Å interval for $T_w = 3000$ K and $\dot{m}_p = 0.3$ kg/m$^2 \cdot$ s.

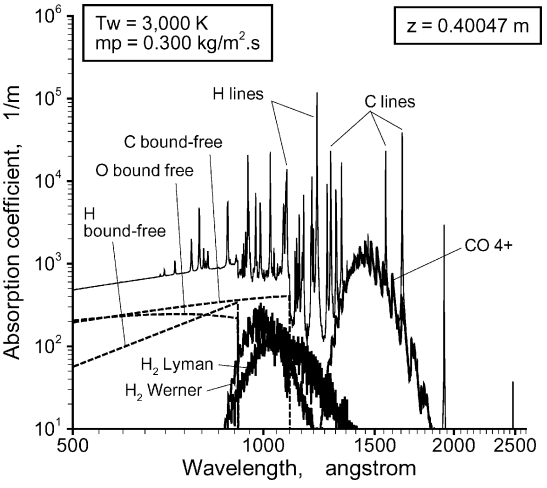

Fig. 12 Spectral distribution of emission coefficient at 0.47-mm distance from wall on stagnation-point streamline for $T_w = 3000$ K and $\dot{m}_p = 0.3$ kg/m$^2 \cdot$ s.

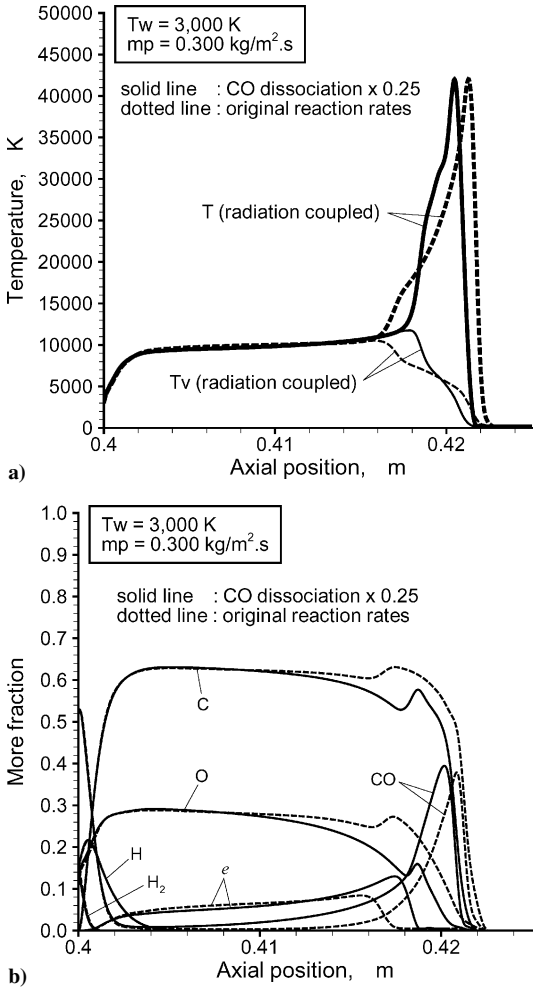

Fig. 13 Influence of CO dissociation rate on distributions of temperatures and chemical components along stagnation-point streamline, $T_w = 3000$ K and $\dot{m}_p = 0.3$ kg/m$^2 \cdot$ s.

B. Tested Results

The stagnation-point heat transfer rates calculated by different rate coefficients are summarized in Table 7. When the CO dissociation rate was slowed down by 0.25, it was necessary to update S_r at every 2000 steps of the CFD calculation to obtain a converged solution. This is because radiative heat transfer had much stronger effects on the shock-layer flow. The decrease of the CO dissociation rate by 0.25 increases the stagnation-point radiative heat flux by 50%, as shown in Table 7. This is because, as shown in Figs. 13a and 13b, the region in which the vibrational–electronic temperature is locally elevated appears behind the shock wave, though concentrations of the illuminant chemical species, C and O, are reduced in this region. The increase of the vibrational temperature is brought about by deceleration of vibrational energy removal along with dissociation in comparison to the vibrational relaxation.

In contrast to the dissociation of CO, changes in rate coefficients for reactions 22 and 23 have only little influence on the stagnation-point heat transfer rate, as seen in Table 7. However, as shown in Figs. 14a and 14b, the rate coefficients taken from Ref. 12 overestimate the concentration of H and C_3 and underestimate that of C, O, CO, C_2, and C_2H on the wall surface. The increase of H and C_3 in the vicinity of the wall increases absorption of the radiative heat flux in vacuum-ultraviolet wavelengths, whereas the decrease of CO and C decreases absorption conversely. For this reason, the small difference between the stagnation-point heat transfer rates calculated by different rate coefficients seems to be accidental.

Note that the rate coefficients for reactions 5, 11, 13, and 21, which may control the distribution of chemical components originating from sublimation of the heatshield and pyrolysis-gas injection, are

Table 7 Stagnation-point heat transfer rates obtained by radiation-coupled and uncoupled calculations for different conditions, in megawatts per square meters

	$\dot{m}_p = 0.3$ kg/m$^2 \cdot$ s[a]				FCW without ablation[b]			
	Uncoupled		Coupled		Uncoupled		Coupled	
Modification	q_c	q_r	q_c	q_r	q_c	q_r	q_c	q_r
CO dissociation rate $\times$ 0.25	4.6	17.5	6.0	12.0	16.3	22.8	16.6	15.2
Rate of reaction 23 from Ref. 12	4.6	11.3	5.3	8.2	——	——	——	——
Rate of reactions 22 and 23 from Ref. 12	4.6	11.3	5.3	8.2	——	——	——	——

[a] $T_W = 3000$ K. [b] $T_W = 300$ K.

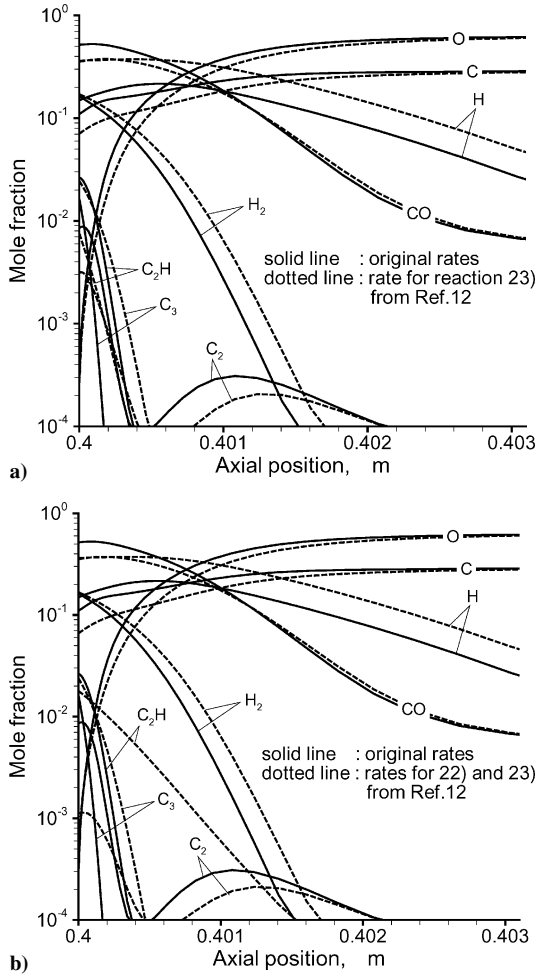

Fig. 14 Influence of rate coefficients for reactions 22 and 23 on distribution of chemical components along stagnation-point streamline, $T_w = 3000$ K and $\dot{m}_p = 0.3$ kg/m$^2 \cdot$ s.

the ones that were only estimated from analogous reactions in Refs. 9 and 12 without experimental verification. To perform more reliable calculations of radiative heat transfer with absorption by ablation gases involved, it is necessary to improve the chemical kinetic models for ablation gases, especially in such flight conditions where the radiative heat transfer plays a dominant role in shock-layer flows.

VI. Summary

An assessment of the stagnation-point heat flux to the Venusian entry capsule in the Venusian trail balloon mission was made at the peak-heating point with the nonequilibrium thermochemistry, ablation, and radiative heat transfer taken into consideration. The radiation code was improved for Venusian entries and radiation-coupled flowfield calculations by a line-by-line method. Considerable influences of radiative heat transfer on thermochemical behavior of the shock-layer flows are found. The convective and the radiative heat transfer rates obtained by radiation-coupled calculation are 13–18% larger and 28–30% smaller than those obtained by uncoupled calculation, respectively. Atomic line spectra of C and O are most responsible for the radiative heat flux. In contras, atomic bound-free transitions and molecular band systems of CO 4+, H_2 Lyman, and H_2 Werner are the dominant sources of continuous absorption in the vicinity of the wall. The rate coefficient of CO dissociation is found to make a significant impact on the computed convective and radiative heat fluxes.

References

[1]Marov, M., and Grinspoon, D., *The Planet Venus*, Yale Univ. Press, New Haven, CT, 1998.

[2]Fabrega, J., Schirmann, T., Schmidt, R., and McCoy, D., "Venus Express—First European Mission to Venus," International Astronautical Congress, Report IAC-03-Q.2.06, Sept. 2003.

[3]Satoh, T., Nakamura, M., Ueno, M., Iwagami, N., Sugita, S., Kasaba, Y., Abe, T., Imamura, T., and Oyama, K., "Japanese Venus Mission, VCO: A Challenge to Answer an Outstanding Question of Planetary Science," American Geophysical Union, Paper P21A-12, 2002.

[4]Yamada, T., Izutsu, N., Fujita, K., and Ishii, N., "Venus Entry Capsule and Balloon Observation," 4th International Symposium on Atmospheric Reentry Vehicles and Systems, CD-ROM, Chapter Missions and Programs, Paper No. 10, The Association Aronautique et Astronautique de France, Vemeuil sur Seine, France, March 2005.

[5]Inatani, Y., "Aerodynamics, Thermophysics, Thermal Protection, Flight System Analysis and Design of Asteroid Sample Return Capsule," Inst. of Space and Astronautical Science Rept. SP 17, May 2003.

[6]Sagdeev, R. Z., Linkin, V. M., Blamont, J. E., and Preston, R. A., "The VEGA Venus Balloon Experiment," *Science*, Vol. 231, March 1986, pp. 1407–1408.

[7]Izutsu, N., Honda, H., Yajima, N., and Imamura, T., "Scientific Ballooning for the Planets: Recent Research Activity of ISAS Balloon Group," Paper 2002-m-11, Proceedings of 23rd International Symposium on Space Technology and Science, Japan Society for Aeronautical and Space Science, Tokyo, 2002, pp. 2043–2048.

[8]Tauber, M. E., Bowles, J. V., and Yang, L., "Use of Atmospheric Braking During Mars Missions," *Journal of Spacecraft and Rockets*, Vol. 27, No. 5, 1990, pp. 514–521.

[9]Park, C., and Ahn, H.-K., "Stagnation-Point Heat Transfer Rates for Pioneer-Venus Probes," *Journal of Thermophysics and Heat Transfer*, Vol. 13, No. 1, 1999, pp. 33–41.

[10]Park, C., Howe, J. T., Jaffe, R. L., and Candler, G. V., "Review of Chemical-Kinetic Problems of Future NASA Missions, II: Mars Entries," *Journal of Thermophysics and Heat Transfer*, Vol. 8, No. 1, 1994, pp. 9–23.

[11]Rock, S. G., Candler, G. V., and Hornung, H. G., "Analysis of Thermochemical Nonequilibrium Models for Carbon Dioxide Flows," *AIAA Journal*, Vol. 31. No. 12, 1993, pp. 2255–2262.

[12]Park, C., Jaffe, R. L., and Partridge, H., "Chemical-Kinetic Parameters of Hyperbolic Earth Entry," *Journal of Thermophysics and Heat Transfer*, Vol. 15, No. 1, 2001, pp. 76–90.

[13]Ahn, H.-K., Sawada, K., and Park, C., "CFD Calculation of Heat Fluxes in Turbulent Flow for Pioneer-Venus Probes," AIAA Paper 98-0833, Jan. 1998.

[14]Izawa, Y., and Sawada, K., "Calculation of Hypersonic Flow with Ablation for Pioneer-Venus Probe," AIAA Paper 2000-0208, Jan. 2000.

[15]Takahashi, M., and Sawada, K., "Simulation of entry Flight Flowfield over Four Prove Vehicles in Pioneer-Venus Mission," AIAA Paper 2002-0909, Jan. 2002.

[16]Fujita, K., and Abe, T., *SPRADIAN, Structured Package for Radiation Analysis: Theory and Application*, Inst. of Space and Astronautical Science Rept. 669, Kanagawa, Japan, Sept. 1997.

[17]Fujita, K., Mizuno, M., Ishida, K., Ito, T., Sumi, T., and Kurotaki, T., "Spectroscopic Diagnostics of Electrically Heated High Enthalpy Wind Tunnels," AIAA Paper 2005-0173, Jan. 2005.

[18]Tsang, W., and Hampson, R. F., "Chemical Kinetic Data Base for Combustion Chemistry. Part I. Methane and Related Compounds," *Journal of Physical and Chemical Reference Data*, Vol. 15, No. 3, 1986, pp. 1087–1279.

[19]Beck, W. H., and Mackie, J. C., "Formation and Dissociation of C_2 from High Temperature Pyrolysis of Acetylene," *Journal of Chemical Society, Faraday Transactions I*, Vol. 71, No. 6, 1975, pp. 1363–1371.

[20]Kruse, T., and Roth, P., "Kinetics of C_2 Reactions during High-Temperature Pyrolysis of Acetylene," *Journal of Physical Chemistry A*, Vol. 101, No. 11, 1997, pp. 2138–2146.

[21]Park, C., *Nonequilibrium Hypersonic Aerothermodynamics*, Wiley, New York, 1990, Chaps. 3, 5.

[22]Hirschfelder, J. O., Curtiss, C. F., and Bird, R. B., *Molecular Theory of Gases and Liquids*, Wiley, New York, 1954, Chap. 7.

[23]Devoto, R. S., "Transport Properties of Ionized Monatomic Gases," *Physics of Fluids*, Vol. 9, No. 6, 1966, pp. 1230–1240.

[24]Capitelli, M., Gorse, C., Longo, S., and Giordano, D., "Transport Properties of High Temperature Air Species," *Journal of Thermophysics and Heat Transfer*, Vol. 14, No. 2, 2000, pp. 259–268.

[25]Levin, E., and Wright, M. J., "Collision Integrals for Ion-Neutral Interactions of Nitrogen and Oxygen," *Journal of Thermophysics and Heat Transfer*, Vol. 18, No. 1, 2004, pp. 143–147.

[26]Potts, R. L., "Application of Integral Methods to Ablation Charring Erosion, A Review," *Journal of Spacecraft and Rockets*, Vol. 32, No. 2, 1995, pp. 200–209.

[27]Wada, Y., and Liou, M. S., "A Flux Splitting Scheme with High-Resolution and Robustness for Discontinuities," AIAA Paper 94-0083, Jan. 1994.

[28]van Lee, B., "Toward the Ultimate Conservative Difference Scheme. 5, A Second-Order Sequel to Godonov's Method," *Journal of Computational Physics*, Vol. 23, No. 1, 1979, pp. 101–136.

[29]Eberhardt, S., and Imlay, S., "Diagonal Implicit Scheme for Computing Flows with Finite Rate Chemistry," *Journal of Thermophysics and Heat Transfer*, Vol. 6, No. 2, 1992, pp. 208–216.

[30]Fujita, K., Sumi, T., Yamada, T., and Ishii, N., "Preliminary Assessment of Venus Entry Capsule Heating Environments," 4th International Symposium on Atmospheric Reentry Vehicles and Systems, CD-ROM, Chapter Aerothermophysics, Paper No. 3, The Association Aronautique et Astronautique de France, Vemeuil sur Seine, France, 2005.

[31]Baulch, D. L., Drysdale, D. D., Duxbury, J., and Grant, S. J., Evaluated Kinetic Data for High Temperature Reactions, Vol. 3, Homogeneous Gas Phase Reactions of the O_2-O_3 System, the CO-O_2-H_2 System, and of Sulphur-Containing Species, Butterworths, London-Boston, 1987.

[32]Mick, H. J., and Roth, P., "High Temperature Thermal Decomposition of CO and CN," *Proceedings of 18th International Symposium on Shock Waves and Shock Tubes*, Springer-Verlag, New York, 1991, pp. 805–812.

[33]Nealy, J. E., "An Experimental Study of Ultraviolet Radiation Behind Incident Normal Shock Waves in CO_2 at Venusian Entry Speeds," AIAA Paper 75-1150, Sept. 1975.

[34]Hanson, R. K., "Shock-Tube Study of Carbon Monoxide Dissociation Kinetics," *Journal of Chemical Physics*, Vol. 60, No. 12, 1974, pp. 4970–4976.